

Buoyant miscible displacement flows in a nonuniform Hele-Shaw cell

E. Walling, R. Mollaabbasi, and S. M. Taghavi*

Department of Chemical Engineering, Université Laval, Québec, QC, Canada G1V 0A6

(Received 26 October 2017; published 29 March 2018)

Miscible displacement flows within the gap of a nonuniform Hele-Shaw cell are considered, theoretically and experimentally. The cell is vertical and it can be diverging or converging. A light fluid displaces a heavy fluid downwards. The displacement imposed velocity is sufficiently large so that diffusive effects are negligible within our time scale of interest. For certain flow parameters, the displacement flow is characterized by a symmetric, two-dimensional penetration of the light fluid into the heavy one, for which a lubrication approximation approach is developed to simplify the governing equations and find a semianalytical solution for the flux functions. The solutions reveal how the cell nonuniformity may affect the propagation of the interface between the two fluids, versus the other flow parameters, i.e., the viscosity ratio (m) and a buoyancy number (χ), for which a detailed flow regime classification is presented. Our results demonstrate that the presence of nonuniformity adds a unique spatiotemporal nature to these displacements which is not the case for uniform cell flows. The combination of the model and experiments reveals the existence of self-spreading, spike, and unstable (viscous fingering) flow regimes, which may occur at various spatial positions within the cell. A converging cell may allow a transition from spike to self-spreading or unstable regime, whereas a diverging cell may offer a transition from self-spreading or unstable to spike regime. Our work demonstrates that the novel spatiotemporal nature of nonuniform cell flows must be considered through the numerical solution of the interface propagation equation, to yield accurate predictions about the flow behaviors at various spatial positions.

DOI: [10.1103/PhysRevFluids.3.034003](https://doi.org/10.1103/PhysRevFluids.3.034003)**I. INTRODUCTION**

The manner by which miscible fluids displace each other in porous media is a key consideration when conceiving and developing various industrial processes. These flows find current use in various applications such as oil well cementing and fixed bed regeneration [1], oil and gas extraction [2,3], and food processing [4] to name a few. An important body of work has searched to understand and unravel the complexity of these flows which present various stable and unstable behaviors depending on a multitude of physical characteristics. So far, a majority of the work on these flows has focused on their behaviors within the confines of uniform geometries, due to their already complex nature. However, displacement flows are much more prevalent in somewhat nonuniform geometries [5]. In this paper, we aim at developing a model, validated by experiments, which can provide a basic understanding of how a small geometry nonuniformity may affect density-stable displacement flows within the gap of a narrow vertical channel.

To this day, the majority of the research into miscible vertical displacements in Hele-Shaw cells has mainly focused on characterizing and modeling the unstable regime observed above critical density or viscosity ratios or above a critical velocity (e.g., see [1,6–12]). Lajeunesse *et al.* [13] studied these

*Corresponding author: Seyed-Mohammad.Taghavi@gch.ulaval.ca

flows through characterizing the effect of viscosity ratio and flow rate. They determined that there exists a two-dimensional phenomenon which occurs under a critical viscosity ratio in density-stable systems. In these conditions, the interface between the fluids progresses from its initially flat state to that of a two-dimensional tongue, as the lighter fluid displaces the heavier one in a vertical Hele-Shaw cell. The tongue is symmetrical with respect to the gap and no instability is observed across the width of the interface. This is in contrast to flows above these critical values which develop into viscous fingers. The authors developed an analytical expression allowing one to determine the boundary between these two flow regimes (stable and unstable). This work was expanded upon by Lajeunesse *et al.* [14], who uncovered three regimes dependent on the viscosity ratio and a buoyancy number; these regimes are characterized by the absence of a shock, the presence of an internal shock, and the presence of a frontal shock. The authors found that each regime had a clearly delineated boundary, with the frontal shock regime being associated mainly with three-dimensional (3D) or unstable behaviors. Further clarification on the boundary expression was provided in [15]. These results were taken into account during later linear stability analyses offered by Goyal *et al.* [16,17].

Modeling of the flow behavior of miscible displacements in the gap of a channel has been undertaken by various authors. Previous to the work of Lajeunesse [14], Rakotomalala *et al.* [18] used the Bhatnagar-Gross-Krook (BGK) lattice gas method to simulate the displacement between parallel plates, predicting the self-spreading regime and the development of a tonguelike flow. Yang and Yortsos [19] concurrently developed an asymptotic formalism to model displacements in between parallel plates and in cylindrical capillaries, which provided a strong basis for future work. More recently, modeling of various relevant flows in channels has been provided by [10,11,20–23], to name but a few. For example, Taghavi *et al.* [20] used a lubrication approximation to predict the flow of buoyancy-driven displacements in parallel channels. Following up on this, Mollaabbasi and Taghavi [23] applied lubrication theory to model these same flows in nonuniform channels. Their results showed that the nonuniformity of the channel affects the local buoyancy force as the flow progresses through the channel. This in turn modifies the interface development throughout the channel. Therefore, it was concluded that, due to the spatiotemporal nature of the interface development, analyzing nonuniform geometry flows requires models that properly take into account the geometrical variations.

Due to the importance that displacement flows present, a growing body of research has searched for methods which would allow one to control them. Thomé *et al.* [24] experimentally examined the impact of nonuniform cells on viscous fingering, concluding that nonuniformity can have considerable impacts on the stability of the flow. Similar results were obtained by [5,25] experimentally; however, Zhao *et al.* [25] noted that this behavior was not predicted through linear stability analysis. An analytical evaluation was later provided by Dias and Miranda [26] who succeeded to predict the stability of the fingers through a perturbative mode coupling theory. Research in this vein has found a growing interest in the past few years, albeit with the primary focus being on viscous fingering of immiscible flows [5,27–36].

To reiterate, the aim of the current work is to theoretically and experimentally explore the impact of a nonuniform Hele-Shaw cell on the displacement in between the gap for density-stable miscible systems. More specifically, we aim at determining the impact of a gap gradient on the three domains identified in the work of Lajeunesse *et al.* [14], using a simple approach that does not constitute a stability analysis. In addition, our work provides an understanding on whether a gap gradient can be used as a tool to control viscous fingering in miscible flows, similarly to immiscible flows. Furthermore, we offer a model, validated by experiments, which provides reasonable predictions of the two-dimensional flow characteristics in a nonuniform channel.

The paper will proceed as follows. In Sec. II, the geometry of the problem, the lubrication model, and the flux function will be discussed. The analytical results are then presented for both uniform and no-uniform cells. Following this, Sec. III is devoted to experiments, detailing the methodology and the results in comparison with the model. Section IV provides a brief summary of the key findings.

II. ANALYTICAL

In our analytical analysis, we consider the two-dimensional shape of the interface between two miscible Newtonian fluids flowing between two plates, separated by small distance $2\hat{D}_0 + 2\tan(\alpha)\hat{x} \approx 2\hat{D}_0 + 2\alpha\hat{x}$ (assuming $|\alpha| \ll 1$). The width and the length of the channel are \hat{D} and \hat{L} , which are both very large compared to \hat{D}_0 . As Fig. 1 illustrates, the two walls of the Hele-Shaw cell are symmetrically oriented with respect to an imaginary vertical line passing through the middle of the channel. We take into account two mechanically stable types of displacement flows: a light fluid displacing a heavy fluid (1) in a slightly converging channel (for negative α) and (2) in a slightly diverging channel (for positive α). The downstream region between the two plates is initially filled with the heavier fluid (fluid H), which is displaced by a lighter fluid (fluid L). The latter is injected at a distance far away from the initial interface between the two fluids localized to $\hat{x} = 0$. The mean imposed velocity is $\hat{V}_0 = \hat{Q}/2\hat{D}_0\hat{D}$, where \hat{Q} is the imposed flow rate of the light fluid. Cartesian coordinates $(\hat{x}, \hat{y}, \hat{z})$ and the geometrical parameters are depicted in Fig. 1. We assume that the displacing fluid interface forms a symmetric tongue across the channel thickness, invariant along the width \hat{D} and characterized by its relative thickness $\hat{h}(\hat{x}, \hat{t})$. The fluids studied are miscible but we consider the large Péclet number limit, the consequence of which is that no significant mixing occurs between the two fluids over the time scales of interest. We have made the Navier-Stokes equations dimensionless using the channel half-thickness at $\hat{x} = 0$ (i.e., \hat{D}_0) as length scale, and \hat{V}_0 as velocity scale. We have scaled time with \hat{D}_0/\hat{V}_0 and pressure and stresses with $\hat{\mu}_H \hat{V}_0/\hat{D}_0$ (with $\hat{\mu}_H$ being the heavy fluid's viscosity). We can therefore write the model equations as

$$[\mp At] \text{Re}[\mathbf{u}_t + \mathbf{u} \cdot \nabla \mathbf{u}] = -\nabla p + \nabla \cdot \tau \mp \frac{\chi}{2} \mathbf{e}_g, \quad (1)$$

$$\nabla \cdot \mathbf{u} = 0. \quad (2)$$

In the equations above, $\mathbf{u} = (u, v, w)$ denotes the velocity, p the pressure, and τ the deviatoric stress. Also $\mathbf{e}_g = (1, 0, 0)$ is in directions (x, y, z) and the \mp refers to the light and heavy fluid layers, respectively, here and elsewhere. Note that we have subtracted the mean static pressure gradient from the pressure before scaling. There are three dimensionless parameters that appear in Eq. (1): the Atwood number defined as $At = (\hat{\rho}_H - \hat{\rho}_L)/(\hat{\rho}_H + \hat{\rho}_L)$ (which is small in our work), the Reynolds

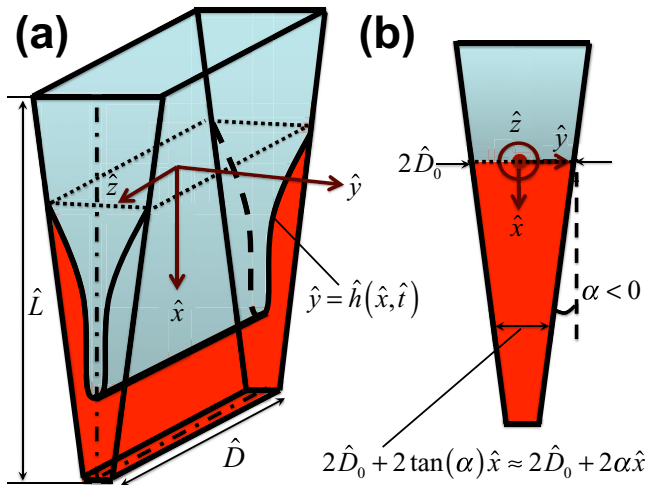


FIG. 1. Schematic of the displacement flow geometry considered. Here α is negative so that the light fluid displaces the heavy fluid in a slightly converging vertical channel. For a positive value of α , the channel would be slightly diverging. Note that $|\alpha| \ll 1$.

number, $\text{Re} \equiv \frac{\hat{V}_0 \hat{D}_0}{\hat{\nu}}$, where $\hat{\nu} = \hat{\mu}_H / \hat{\rho}$ is defined using the mean density $\hat{\rho} = (\hat{\rho}_H + \hat{\rho}_L)/2$, and the buoyancy number can be defined as

$$\chi = \frac{2At \hat{g} \hat{D}_0^2}{\hat{\nu} \hat{V}_0}, \quad (3)$$

which represents the balance of viscous stresses (due to the imposed flow) and axial buoyancy stresses (due to the density difference).

Usual assumptions include no-slip conditions and the channel being sufficiently long in direction x . Thanks to our scaling, we can have in each cross section of the channel

$$\frac{1}{D} \int_{-D/2}^{+D/2} \int_0^{1+\alpha x} u \, dy \, dz = 1. \quad (4)$$

The light fluid may be expected to propagate in the middle of the channel, fingering through the heavier fluid. An interface, denoted by $y = h(x, t)$, separates the two pure fluids (see Fig. 1). We assume that the interface is single valued.

A. Lubrication model

Assuming that the interface is elongated and inertia is not dominant, a thin-film/lubrication style model can be developed for our displacement flow using standard procedures. The leading order equations are the momentum balances:

$$0 = -\frac{\partial p}{\partial x} + m^\mp \frac{\partial^2 u}{\partial y^2} \mp \frac{\chi}{2}, \quad (5)$$

$$0 = -\frac{\partial p}{\partial y}, \quad (6)$$

$$0 = -\frac{\partial p}{\partial z}, \quad (7)$$

where $m^+ = 1$ and the viscosity ratio is defined as $m^- = m = \mu_L / \mu_H$, which is the ratio of the viscosity of the light fluid to that of the heavy fluid. The above equations imply that $p = p(x, t)$. Therefore, for each fluid layer we can write

$$0 = -\frac{\partial p}{\partial x} + m \frac{\partial^2 u}{\partial y^2} - \frac{\chi}{2}, \quad y \in (0, h), \quad (8)$$

$$0 = -\frac{\partial p}{\partial x} + \frac{\partial^2 u}{\partial y^2} + \frac{\chi}{2}, \quad y \in (h, 1 + \alpha x). \quad (9)$$

The boundary conditions are the flow symmetry, leading to $\frac{\partial u}{\partial y} = 0$ at $y = 0$, and no-slip condition ($u = 0$) at the channel wall ($y = 1 + \alpha x$). At the interface between the two fluids ($y = h$) the velocities and shear stresses are continuous. These conditions allow for the determination of u for a given pressure gradient, while the additional constraint (4) is satisfied to determine the pressure gradient. The interface is advected via a kinematic condition, which in combination with the incompressibility condition results in

$$\frac{\partial h}{\partial t} + \frac{\partial q}{\partial x} = 0, \quad (10)$$

where q is defined through

$$q = \frac{1}{D} \int_{D/2}^{D/2} \int_0^h u \, dy \, dz. \quad (11)$$

Regarding boundary conditions, we assume that the channel is full of pure fluid L and fluid H at its two ends. Concerning initial conditions, we must consider an initial profile compatible with the far-field conditions, leading to

$$h(x,0) \rightarrow 1 + \alpha x - H(x)(1 + \alpha x). \quad (12)$$

Here $H(x)$ is the usual Heaviside function, used to ensure that the initial variation in h localized to $x = 0$ is sharp. Note that, in order to conform to the inlet and exit conditions, we need to always limit the length of the channel in a way that the channel walls never contact each other. Thus, for a diverging channel (positive α) we limit the length to $x \in (-\alpha^{-1}, \infty)$ and for a converging one (negative α) to $x \in (-\infty, -\alpha^{-1})$. Hereafter, for simplicity we may refer to x as *distance*, providing a measure of a distance from $x = 0$, the spatial location of the initial interface.

In order to compute the flux function, a great deal of simplicity is achieved through using an analogy between uniform and slightly nonuniform channel flows: as the flow advances in a nonuniform channel, different heights of an imaginary uniform channel are locally achieved. Therefore, we can adopt appropriate scaling and, for a given αx , use the local channel half-thickness [$\hat{D}_0(1 + \alpha x)$] and the local mean flow velocity [$\hat{V}_0/(1 + \alpha x)$] to rescale the dimensionless groups:

$$h^*(\alpha x) = h(1 + \alpha x)^{-1}, \quad (13)$$

$$\chi^*(\alpha x) = \chi(1 + \alpha x)^3, \quad (14)$$

where the rescaled dimensionless groups are denoted by $*$. Note that the values of the local Reynolds number and viscosity ratio are not affected by the nonuniformity. Therefore, the analytical solution for the flux function can be easily found as

$$q = \frac{1}{12} \frac{h^{*2}(1 - h^*)^3 [4h^* + 3m(1 - h^*)] \chi^*}{m(h^{*3} - 1) - h^{*3}} - \frac{1}{2} \frac{h^* [2h^{*2} + 3m(1 - h^{*2})]}{m(h^{*3} - 1) - h^{*3}}. \quad (15)$$

It is important to note that even though an analogy exists between the uniform and nonuniform dimensions, a nonuniform channel remains a completely novel situation which must be addressed as such. Uniform cell flows develop and attain a relatively steady behavior once the flow has progressed, whereas nonuniform cell flows are time and position dependent due to the nature of their constantly changing balancing forces throughout the interface.

Using appropriate boundary conditions, we have solved the interface propagation equation (10) to obtain the interface evolution. We have taken the initial interface as a sharp boundary between the phases. We have discretized the equation in conservative form, first order explicitly in time and second order in space, and employed a shock capturing Van Leer flux limiter scheme [37]. Further details of our numerical approach can be found in our recent displacement flow studies [23,38]. We have checked the independency of our results on the mesh size, as showcased in Fig. 2(a).

B. Uniform cell results

Let us first review certain basic displacement flow features in a uniform channel, which may help better understand the effect of geometry on displacements in a nonuniform channel. In addition, uniform channel results will serve as benchmarks for nonuniform channel counterparts.

Figure 2 depicts displacement flow behaviors for a uniform channel. Due to the symmetry of the flow, the results for half of the channel are shown throughout the paper. Figure 2(a) corresponds to a less-viscous more-viscous displacement ($m = 0.1$) and weak buoyancy ($\chi = 1$). Starting from an initially sharp interface, the interface quickly adopts a form with two segments: A frontal shock, with constant front height (h_f) with a speed larger than a corresponding channel center-line velocity in a Poiseuille flow (i.e., $V_c = 1.5$) and a stretched region between h_f and $h = 1$, which is seemingly pinned to the wall. Figure 2(b) shows another flow regime in which the sharp interface (at $t = 0$) transitions into a form with three segments, two of which are similar to Fig. 2(a). The third interface

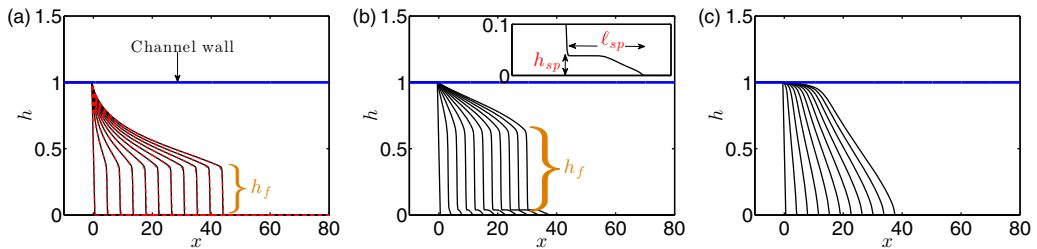


FIG. 2. Examples of displacements showing interface evolution in time at $t = 0, 2.5, \dots, 22.5, 25$, for (a) $m = 0.1$, $\chi = 1$; (b) $m = 1$, $\chi = 10$; (c) $m = 10$, $\chi = 1$. In (a), the convergence of the results is shown using two typical mesh sizes: $dx = 0.1$ (line) and $dx = 0.2$ (dashed line). The inset for (b) is zoomed at the displacing tip in the range $25 \leq x \leq 40$. Also, note that h_f , h_{sp} , and ℓ_{sp} denote the front height, the spike height, and the spike length.

segment is an advancing foot (spike) localized toward the channel center line. The shock moves slower than the tip of the spike and therefore the spike length (ℓ_{sp}) increases with time. After forming, the spike height with respect to the channel center line (h_{sp}) seems to be constant. Figure 2(c) illustrates an example of the last regime, which is a self-spreading interface motion occurring at large viscosity ratios and weak buoyancy. There is no shock or spike observed in this regime.

The numerical solution of the interface propagation equation delivered the interface evolution versus time and space. However, for a uniform channel, the flux function can be directly analyzed to provide a flow regime classification, without the need for a numerical solution. This has been extensively carried out by Lajeunesse *et al.* [14], who analytically discovered the three displacement flow regimes which we briefly reviewed. To define these regimes, let us rely on the following *simplistic* terms:

(1) *Self-spreading flow*: This flow regime is associated to self-spreading interface profiles across the channel. The tip of the interface moves with the same speed as the channel center-line velocity in a corresponding Poiseuille flow (V_c).

(2) *Spike flow*: In this flow regime, interface profiles involve an internal shock, across two interface values. The shock is preceded by an advancing, self-spreading foot (spike), the tip of which propagates at the same speed as V_c and the shock travels at a velocity smaller than V_c .

(3) *Frontal shock flow*: This corresponds to a flow regime with no leading foot (spike) and with a shock at the front of the displacing fluid, traveling with a speed equal to or larger than V_c .

Through analyzing the flux function, Lajeunesse *et al.* [14] were also able to quantify the transition between the regimes discussed above. In addition, they found very good comparisons between their model results and experimental results for the first two regimes. However, the experimental flows corresponding to the parameter ranges of the third regime did not match with the theory: the experimental interface profiles had either a front velocity smaller than the corresponding model profiles (for a limited range of parameters) or they showed three-dimensional fingering patterns. Lajeunesse *et al.* [14] showed that the critical upper limit (in terms of the buoyancy number χ) for the onset of the transition toward three-dimensional instabilities is crudely equivalent to the onset of the transition between spike and frontal shock flows obtained by the model. They argued that a shock velocity larger than the maximum velocity existing in the displaced fluid ahead of the interface introduces a vorticity, leading to recirculation at the interface tip, which acts as the origin of the observed interfacial instability. This will eventually expand to 3D behaviors observed in the channel transverse direction. Our results will show that the same criterion can be used to crudely delineate the transition between stable and unstable flows in a nonuniform channel, although there is no shortcut to analytically obtain the associated critical conditions. Instead, the interface propagation equation needs to be numerically solved to deliver the transition boundary.

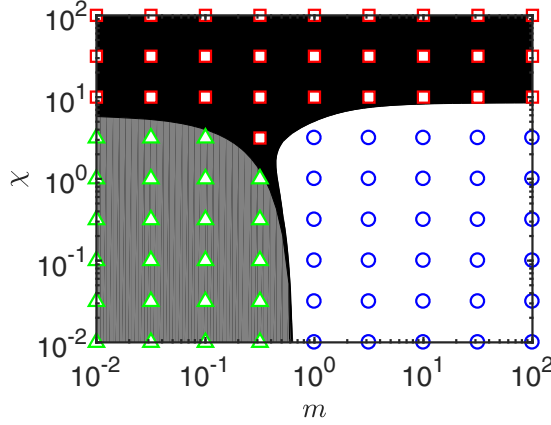


FIG. 3. Comparison between analytical regime classification for uniform Hele-Shaw cell displacement flows and simulation results of the spike (\square), self-spreading (\circ), and frontal shock (\triangle) regimes. The boundaries between the regimes, marked by different colors, can be obtained by analyzing the analytical form of the flux function, for which the details can be found in [14]. Throughout the paper, we adopt the convention of denoting simulation and experimental datapoints by hollow and filled symbols, respectively.

In order to validate our results against those of [14] for a uniform channel, Fig. 3 shows the regime classification for the three regimes discussed above. The simulation results superposed on the graph reasonably match the predictions of the regimes and their boundaries using the method proposed by [14]. This is an important validation step since, in analyzing the nonuniform channel displacements in the following sections, we will rely on simulation results as analytical treatments are not possible.

Before we proceed, it is useful to quantify certain flow features for the displacement flow regimes discussed. For example, it can be shown that the overall displacement efficiency is governed by the shock speed and height in frontal shock and spike flows. In order to approximate these quantities, the mass conservation of the total volume behind the interface results in

$$h_f \left. \frac{\partial q}{\partial h} \right|_{h=h_f} = q(h_f), \quad (16)$$

where h_f is the front height, with which the front speed can be found as $V_f = \left. \frac{\partial q}{\partial h} \right|_{h=h_f}$. Note that in deriving relation (16), we have assumed that the area under the spike in the spike regime is relatively small and therefore negligible. For the frontal shock regime, Eq. (16) involves no approximation. After some algebra, the shock speed can be found as

$$V_f = \frac{(1 - h_f)}{4[(m - 1)h_f^3 - m]^2} \left\{ \chi [(3m^2 - 7m + 4)h_f^7 - (5m^2 - 9m + 4)h_f^6 + (m - 1)mh_f^5 + (-5m + 7)mh_f^4 + (14m - 12)mh_f^3 + (4 - 10m)h_f^2m + 2h_fm^2] - 6m(m + h_fm - 2h_f^2 + 2h_f^2m) \right\}, \quad (17)$$

in which the buoyancy number and the shock height are linked through

$$\chi = \frac{6h_f[h_f^3(2 - 5m + 3m^2) + 9h_fm(1 - m) + 2m(3m - 2)](h_f - 1)^{-2}}{[2h_f^5(3m^2 - 7m + 4) + 2h_f(2h_f^3 + 3mh_f^2 - 4m)(1 - m) + 5h_f^2m(4 - 3m) - 3m^2]}. \quad (18)$$

For the frontal shock regime and when $V_f > V_c$, the values of V_f and h_f provided by the coupled equations (17) and (18) are of less importance since they are not physically relevant (i.e., this regime is not observed in experiments). However, these equations can help provide the transition

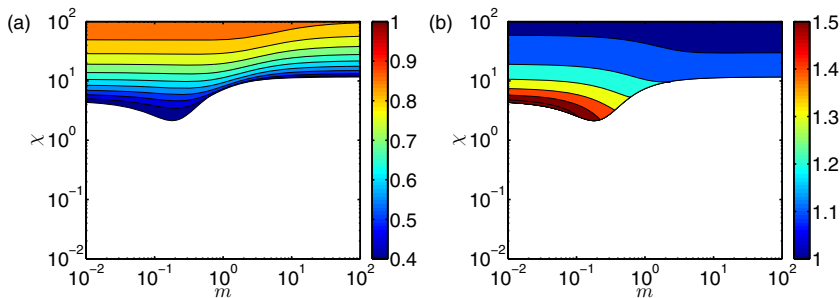


FIG. 4. Results for a uniform channel. (a) Contours of h_s versus χ and m . (b) Contours of V_f versus χ and m .

between the spike and frontal shock regimes, obtained through requiring $V_f = V_c$, which results in a critical buoyancy number $\chi_c = \frac{3}{8}(-2 + 3m)^2(4 - 3m)$, which marks the boundary between these two regimes in Fig. 3. On the other hand, the boundary between self-spreading and shock flows (also marked in Fig. 3) can be found by requiring a single inflection point on the flux function.

For spike flows, the coupled equations (17) and (18) approximate the shock height and speed. Figure 4 depicts contour plots of h_f and V_f in the plane of χ and m , for the spike regime. It can be seen that h_f and V_f are strongly affected by χ and that h_f is less affected by m , while the effect of m on V_f is more visible.

C. Nonuniform cell results

A nonuniform channel flow presents a spatiotemporal nature (nonexistent in a uniform channel), due to the continuous change in local buoyancy affecting the interface along its length. Unlike a uniform channel with a relatively steady behavior, the nonuniform channel transitory nature implies that the overall flow behavior is subject to the accumulation of local buoyancy forces acting throughout the interface. Therefore, the flow behavior prediction requires the solution of the interface propagation equation, taking into account the spatiotemporal nature of the flow, and cannot simply be obtained from a conversion of solutions obtained in uniform channels. As further discussed below, we must therefore proceed by numerical simulation. Figure 5 compares displacement flows in nonuniform channels (converging and diverging) with the ones in uniform channels, for various viscosity ratios and a given buoyancy number (fixed at $\chi = 10$) at small α . Interesting behaviors appear when the channel is nonuniform. For example, Fig. 5(a) shows that the shock height (speed) decreases (increases) with distance as the front advances, which is expected. In this case, as a less viscous fluid displaces a more viscous one ($m = 0.1$), the initially flat interface quickly turns into a shock at the front. However, before a frontal shock is formed, a short-lived spike appears near the front at intermediate values of x . Although the spike slightly grows initially, as the local buoyancy stress decreases with x , it eventually fades away. Figure 5(b) shows a spike regime, wherein the spike's longitudinal length grows, and the shock that follows the spike has a constant height (both expected features). Also, the height of the spike seems to be constant. Figure 5(c) illustrates a displacement flow in a diverging channel, with flow behaviors that are opposite to those in a converging case. There is a growing spike formed at the front and there is a succeeding shock, for which the height (speed) increases (decreases) with x . The middle row in Fig. 5 shows displacements at $m = 1$. Regarding Figs. 5(e) and 5(f), the general flow behaviors are more or less similar to the corresponding subfigures in the top row. However, Fig. 5(d) shows a different pattern, wherein the initial flat front interface quickly turns into a spike regime with a shock that follows the front. As the spike grows and the shock height decreases, the interface is extended between a pinned point on the top wall and the tip at the bottom. The shock becomes weakened and at a certain distance the flow transitions to self-spreading regime. The bottom row depicts the results for $m = 10$, where Fig. 5(g) shows an

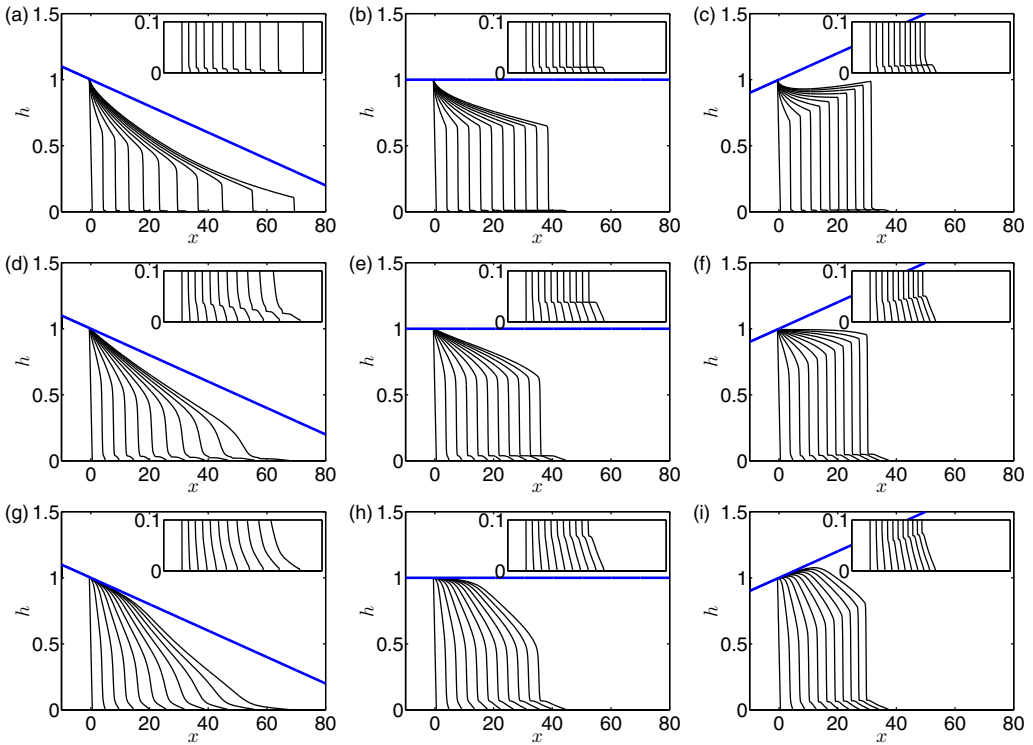


FIG. 5. Interface evolution in time, $t = 0, 3, \dots, 27, 30$ at $\chi = 10$. In each row m is fixed ($m = 0.1, 1, 10$ from top to bottom). In each column, α is fixed ($\alpha = -0.01, 0, +0.01$ from left to right). The insets show interface heights close to the tip and cover the same range of x as in the main figures.

even faster transition from spike to self-spreading regime. Figures 5(h) and 5(i) show more or less the same pattern as the corresponding subfigures in the top and middle rows, although a relatively faster spike height growth can be noted in Fig. 5(i).

Before we proceed with the presentation of our experimental results in the following section, let us address a natural question that may arise: To what degree can the results from a uniform channel analysis be extended to understand the flow in a nonuniform channel? More precisely, using the transformation introduced as relation (14), can the transition between different regimes in a nonuniform channel be directly obtained from the analysis of a uniform channel flow? Our results show that “in general” the answer to these questions is negative, meaning that, due to the spatiotemporal nature of the flow in a nonuniform channel, the interface propagation equation must be solved for individual cases to obtain the transition boundaries for nonuniform channel flows. For clarification, Fig. 6(a) shows the simulation results of the variation of the critical scaled buoyancy number [i.e., $\chi_{cr}^* \equiv \chi_{cr}(1 + \alpha x)^3$] versus αx . To obtain this figure, several hundred simulations have been performed to quantify the critical buoyancy number that delineates the transition between spike to self-spreading regime or spike to shock regime, for a wide range of m and αx . The datapoints at $\alpha x = 0$ represent the uniform channel results. For each viscosity ratio and any $\alpha x \neq 0$, the values of χ_{cr}^* deviate from the corresponding values at $\alpha x = 0$, implying that the uniform channel results cannot be directly extended to nonuniform channel results. In general, major deviations are observed for small viscosity ratios with the transition from spike to shock in converging channels. For large viscosity ratios, for which the transition from spike to self-spreading occurs, increasing m generally results in decreasing the deviation from uniform channel results; for example, at $m = 10$, the simulation datapoints seem to be least deviated from an imaginary horizontal line (for which

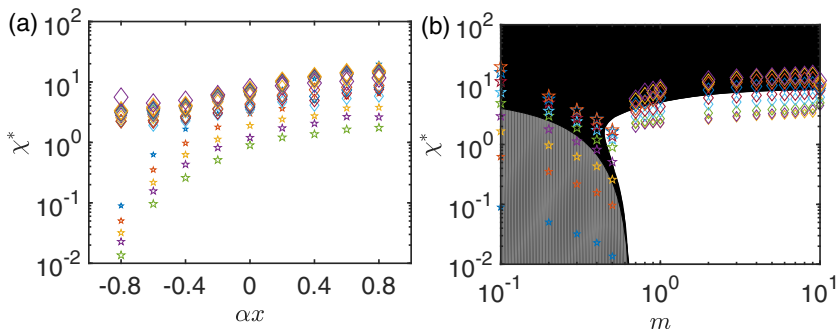


FIG. 6. Simulation datapoints representing $\chi_{\text{cr}}^* \equiv \chi_{\text{cr}}(1 + \alpha x)^3$, denoting the critical buoyancy number for the transition from spike to self-spreading regime (diamonds) and the transition from spike to frontal shock regime (stars). (a) Critical values in the plane of χ^* and αx . The symbol size represents the viscosity ratio magnitude, varying as $m = 0.1, 0.2, \dots, 1, 2, \dots, 9, 10$, except for $m = 0.6$ which is undetermined due to it being the zone in between self-spreading and shock flows. (b) Critical values in the plane of χ^* and m . The symbol size represents the growth in αx , varying as $\alpha x = -0.8, -0.6, \dots, 0.6, 0.8$. The shaded areas mark the regimes predicted by the analytical results for uniform cells, i.e., the same as presented in Fig. 3. Note that nonuniform cell results cannot necessarily be extended from uniform ones since the critical values for nonuniform cells vary with αx in (a) and they do not collapse on uniform cell boundaries in (b).

χ_{cr}^* would be independent of αx). Figure 6(b) provides the same simulation results as presented in Fig. 6(a), but in the plane of the scaled buoyancy number versus the viscosity ratio. This figure is analogous to Fig. 3 in terms of regime classification while it quantifies the critical transition boundaries for nonuniform channels.

III. EXPERIMENT

A. Method

Experiments in uniform and nonuniform Hele-Shaw cells were carried out to provide comparisons with our model results. The experiments for the uniform geometry were performed in a Hele-Shaw cell of 80 cm length, 10 cm width, and a gap of 1.8 mm. The cell was built of two $90 \times 15 \times 2.4$ cm³ clear polyacrylic sheets; a large thickness being necessary to prevent any bowing in the sheets. The gap between the sheets was achieved by placing a rubber lining around the 80×10 cm² zone through which the fluids flow. The sheets were compressed using C-clamps at regular intervals to ensure even compression and an airtight seal. The same process was undertaken for the nonuniform geometry, the only difference being that multiple acrylic sheets were machined to achieve a groove of varying depth around the zone of flow to produce a nonuniform cell of 1.8 mm gap on one end and 1 or 0.6 mm gap on the other. The cell was supported by a metal frame which offered lateral and vertical support.

Distilled water was employed as a base for most of the solutions used in the course of the experiments. Sodium chloride (NaCl) was favored as a weighting agent to increase the density of the fluids. A high precision density meter (Anton Paar DMA 35) was used to measure the density of the solutions before every experiment. Ambient temperature was maintained at $24 \pm 1^\circ$ for all experiments. The viscosity ratio was controlled using water-glycerol solutions, for which the initial estimations were based on the work of [39], also confirmed using a digital controlled shear stress–shear rate rheometer (AR-G2 TA Instrument).

For illustration purposes, the displacing fluid was always colored using Fountain Pen India black ink, whereas the displaced fluid was kept translucent. The experiments were filmed using a monochromatic camera (Basler acA2040, with 4096 gray-scale levels), capturing images in the \hat{x} - \hat{z} plane (see Fig. 1) of the cell backlit by light-emitting diodes. The camera frame rate varied

TABLE I. Experimental flow parameter ranges. The viscosity ratio varied between 0.05 and 10, but was mainly at values of 0.1, 1, and 10. The density of the water-glycerol solution was kept constant at around 1160 kg/m^3 .

αL	$At \times 10^{-3}$	\hat{V}_0 (mm/s)	χ	Re
0	1–50	1–130	0.1–86	1–90
–0.5	1–60	1–85	0.1–726	0.1–77
0.8	1–60	1–220	0.01–1512	0.1–90
–0.8	10–51	1–110	0.9–172	0.1–76
2.5	0.008–0.05	2–330	0.06–1	0.07–0.7

typically in the range of 1–10 fps, depending on the flow rate of the experiments. Light absorption calibrations were performed in usual fashion.

For each experiment, the cell was initially filled with the displaced fluid from the bottom of the cell through an elevated reservoir using gravity, typically up to 10 cm from the top of the cell. The displacing fluid was then introduced through the top of the cell from a reservoir. To obtain a flat and horizontal interface between the fluids and to limit any diffusion and mixing, the injection rate at this stage was maintained low, usually below 1 ml/s (taking around 10 min). Minimal diffusion was impossible to avoid ($< 1 \text{ mm}$), but higher density and viscosity differences allowed one to minimize the diffusion. Overall, the diffusion seems to have had no bearing on the concentration profiles obtained. To start the experiment, the displacing fluid was then injected at a constant flow rate, controlled by needle valves. The flow rate was measured by three methods: a variable area flow meter was used at the entry (top) of the cell, the volume of the liquid at the exit (bottom) was measured with respect to time, and the total volume of the exit fluid was weighed. Experimental ranges are presented in Table I. The experiments occurred at high Péclet number ($Pe = 2\hat{V}_0\hat{D}_0/\hat{D}_m \gg 1$, where \hat{D}_m is the molecular diffusion coefficient), to allow for a well-defined interface between the fluids and to limit mixing. Particularly, the majority of our experiments were performed at $Pe > 10^4$. The slowest flows, with Pe 's of $O(10^3)$, were not considered during analysis to avoid any possible error from mixing or diffusion.

The image processing was carried out using in-house MATLAB codes, which delivered the interface evolution versus time and position, for stable flows.

B. Uniform cell results

Our model results showed the existence of self-spreading, spike, and frontal shock regimes. While self-spreading and spike flows appeared in our experiments, the majority of our experiments did not show any signs of frontal shock characteristics. Instead, unstable flows (typically with the viscous fingering instability) appeared in our experiments for the flow parameters for which the simulation results would have predicted a frontal shock regime. Therefore, experiments were classified according to three domains: self-spreading, spike, and unstable flows, as presented in Fig. 7. We observe a sound agreement between experimental results and the theoretical boundaries. In general, the regimes also concord with the findings of [14,15]. In this figure, the insets depict displacement flow snapshots and the associated interface profiles for the spike and self-spreading domains. In the frontal shock domain, viscous fingering is observed, which manifests itself as linear fingers at large χ but transitions to less stable nonlinear fingers as χ decreases.

Figure 8 compares the experimental results with those obtained from the model, for $m = 1$, in the spike regime. In general, good agreement between the experimental and model results is observed, although the model seems to slightly overestimate the front heights at larger χ .

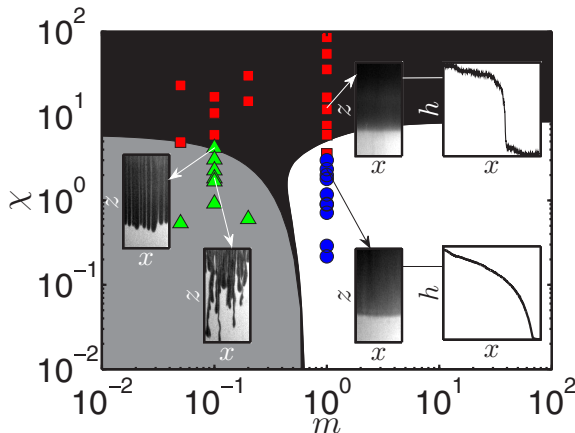


FIG. 7. Experimental results in uniform channels: spike (■), self-spreading (●), and unstable (▲) flows. The shaded areas mark the regimes predicted by the analytical results, as discussed in the analytical section. The field of view for all the inset images is $6 \times 7.5 \text{ cm}^2$. Note that flows in the range of frontal shock (predicted by the model) are unstable flows in experiments.

C. Nonuniform cell results

Now let us turn to the nonuniform cell results. Let us start with a qualitative comparison of interface evolutions in experiments and simulations, as depicted in Fig. 9. In the experimental converging cell, the front height (speed) increases (decreases) while the opposite is true for the diverging cell. The comparison between the theoretical and experimental results seems reasonable for both cases. It is interesting to note that, for the converging geometry, the self-spreading profile initially progresses from spike to self-spreading but eventually evolves into a wedge shape (i.e., a pattern not observed in uniform cells). This wedgelike flow presents a distinct lack of a front and is very prevalent for low buoyancy flows.

An important comparison of the experimental and model results consists of evaluating whether the flow regimes can be properly predicted. To do so, simulations were performed to determine the boundary between the regimes, in the plane of χ^* and αx . Experimental results were subsequently placed on these maps. Figure 10 showcases these results at three viscosity ratios ($m = 0.1, 1,$ and 10), where the simulation predictions agree well with the experimental results. We observe a general behavior as a function of αx wherein a converging geometry slightly increases the extent of the spike domain against either self-spreading or unstable flows, whereas the opposite can be said of

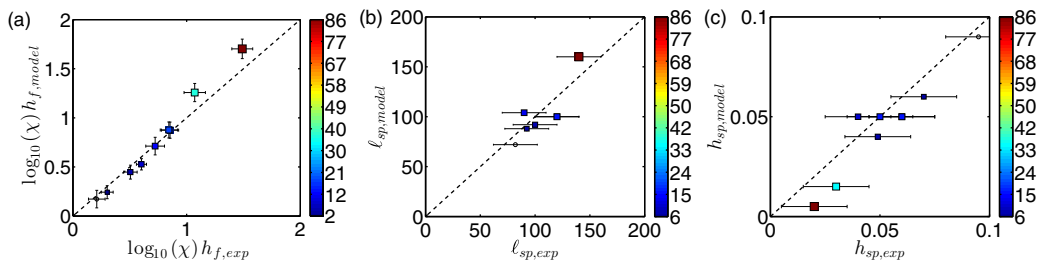


FIG. 8. Simulated versus experimental results for the front height as well as the spike length and height, in a uniform channel for $m = 1$ and measured at $x = 650$. The color bar represents the buoyancy number (χ), here and elsewhere. The axes of some plots are multiplied by $\log_{10}(\chi)$ to offer a better distribution of data.

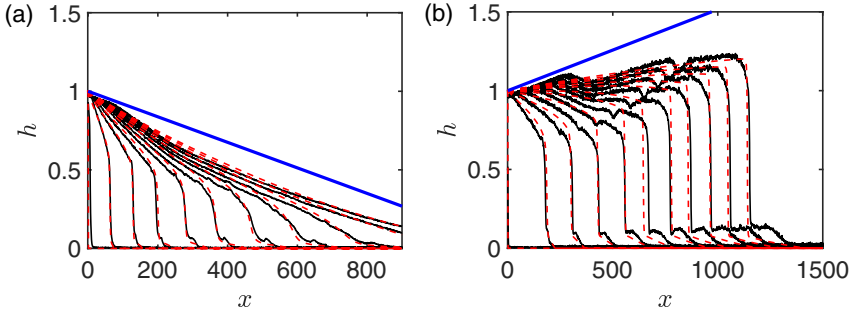


FIG. 9. Experimental results (lines) compared to simulation outputs (dashed lines) for $m = 1$: (a) $\chi = 11$, $\alpha L = -0.8$, $t \approx 0, 50, 100, \dots, 500$; note that due to the progressive decrease in buoyancy, the front height disappears after a certain distance and the self-spreading flow now takes on a shape analogous to a wedge; (b) $\chi = 8$, $\alpha L = 2.5$, $t \approx 0, 130, 230, \dots, 1300$.

the diverging geometry. Perhaps, a more interesting finding arrives when comparing the transition boundaries at different viscosity ratios. First of all, the boundaries for the uniform cell ($\alpha x = 0$) only very weakly depend on m . Second, the boundaries for the diverging cell weakly depend on αx . Finally, the boundaries in the converging cell vary greatly with both m and αx . This is most obvious when comparing the boundaries for $m = 0.1$ and $m = 10$. Compared to higher viscosity ratio flows, our simulations (in Fig. 6) showed that the flows with low viscosity ratios ($m < 0.6$) are more affected by the cell nonuniformity (especially when $\alpha x < 0$, i.e., a converging cell). Figure 10 provides an experimental confirmation of this behavior, showing that the transition boundary for $m = 1$ and 10 only slightly depends on αx , but for $m = 0.1$ greatly varies with αx . One reason for this difference in behavior lies in the fact that the boundary for large m is related to the transition between spike and self-spreading regimes while the boundary for small m concerns the transition between spike (stable) and shock (unstable) regimes. Our findings imply that the displacement flow spatiotemporal nature becomes more relevant in the case of the latter.

The variation in the local buoyancy leads to behaviors that are not present in uniform cells: the flow can now change regime throughout the length of the cell. Figure 10 offers a good overview of this phenomenon. For example, depending on their buoyancy, some flows can start off self-spreading (at $\alpha x \approx 0$) and end up in a spike regime at $\alpha x = -0.8$, or vice versa if the cell is diverging. This phenomenon becomes much more prominent for flows with $m < 0.6$, for which the transition between stable and unstable flows takes place. Therefore, in a converging cell the flow can progress

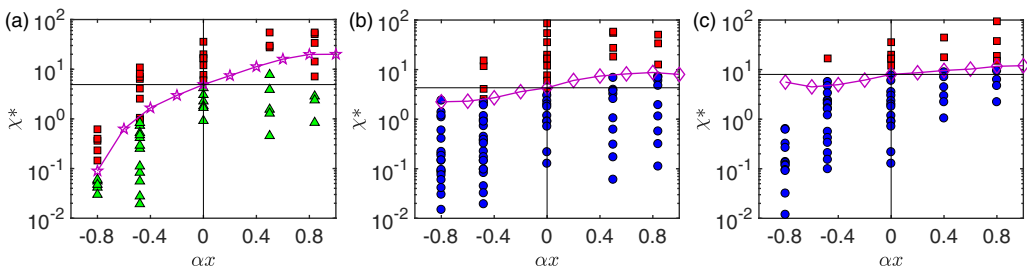


FIG. 10. Experimental results of spike (■), self-spreading (●), and unstable (▲) flows compared to the transition from spike to frontal shock regime (stars and lines) and the transition from spike to self-spreading regime (diamonds and lines), predicted by simulations for $m = 0.1, 1, 10$ (from left to right). In each graph, the intersecting line represents the boundary of the uniform geometry. This figure presents the new domain classification offered for nonuniform flows, analogous to the classification provided in Fig. 7.

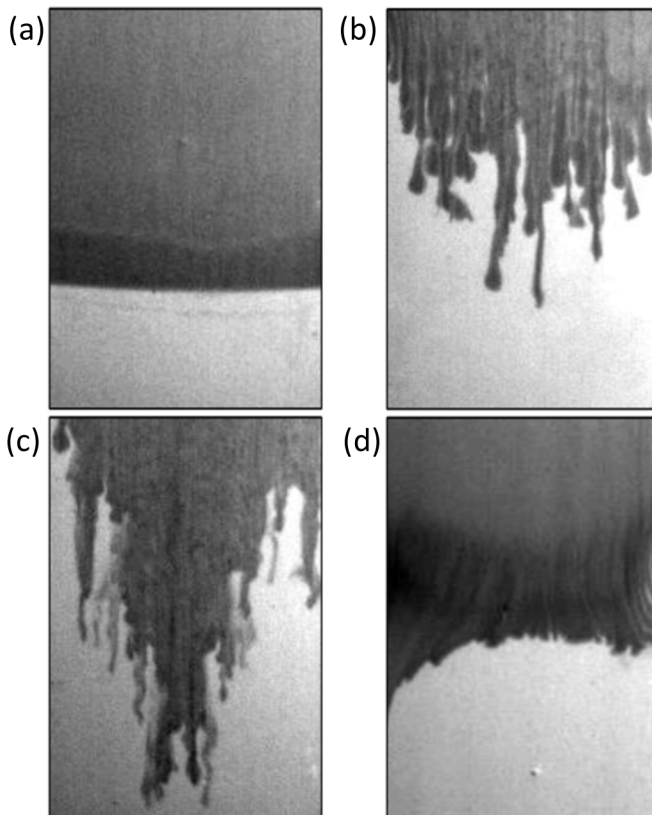


FIG. 11. Experimental results at $m = 0.1$. Top row: (a) a stable interface in a uniform cell compared to (b) a destabilized interface in a converging cell ($\alpha L = -0.8$), both at $\chi = 7.5$. Bottom row: (c) an unstable interface in a uniform cell compared to (d) a stabilized interface in a diverging cell ($\alpha L = 2.5$), both at $\chi = 1$. The field of view is $8.5 \times 12.4 \text{ cm}^2$ in each image.

from spike to self-spreading (or spike to unstable), due to the progressive decrease in local buoyancy promoted by the nonuniformity. The manifestation is similar in a diverging cell wherein the local buoyancy increases and therefore it is possible to transition from unstable or self-spreading to spike regime. Even though the transition between self-spreading and spike regimes can be of interest when seeking to control displacement efficiency, the transition between unstable and spike flows may offer a more alluring consequence: the control of viscous fingering. Our findings show that a converging cell promotes viscous fingering while a diverging cell inhibits it. For a better understanding, flow snapshot examples with comparable buoyancy numbers are presented in Fig. 11. It is clear from the images that, although the mechanisms by which these actions (stabilization or destabilization) occur are the same, they are expressed somewhat differently in converging or diverging cells.

Based on our discussion above, in the converging cell case, the flow would theoretically transition from spike to unstable flow regime at a critical longitudinal distance, due to the decreasing buoyancy. The model predicts a relatively clear transition from one domain to the other. This appears to be more or less the case experimentally as well, while experiments can also help understand how this transition takes place. For the diverging cell case, the flow may transition from unstable to spike regime, meaning that the flow is initially unstable and becomes stabilized at a given αx . The stabilization effect is due to the increase in buoyancy, which halts the progression of the viscous fingers. Experiments demonstrate a consistent pattern on this progressive stabilization. Figure 12 illustrates an example experiment with the images showing this progression and Fig. 13(a) offers further quantification, to

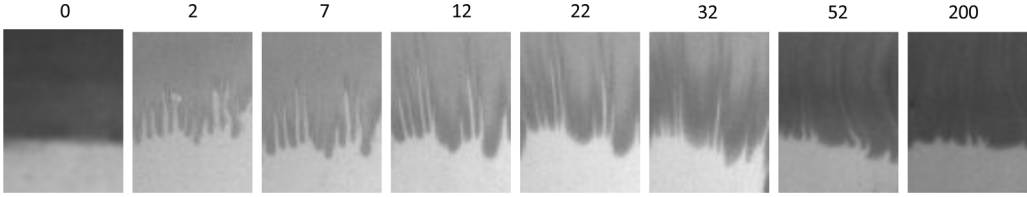


FIG. 12. Snapshots of displacements in a frame that moves with the front. Initial destabilization of the interface followed by stabilization of the flow in a diverging channel of $\alpha L = 2.5$ with $\chi = 0.6$ and $m = 0.1$ for $\hat{t} = 0, 2, 7, 12, 22, 32, 52, 200$ s. The field of view is 3×4 cm².

quantify the number, width, and length of fingers. Figure 12 shows a progressive increase in both the length and width of the individual fingers over time. The number of fingers decreases as the flow progresses and the fingers merge together until local buoyancy forces the few remaining fingers to shorten. The flow finally transitions to a spike regime. A displacement flow with the same parameters in a uniform cell would be very unstable. Figure 13(b) provides the interface evolution corresponding to the same experiment. The simulation quantifies that the transition from frontal shock (unstable) to spike regime (stable) for this case occurs at $x \approx 800$, which is nearly perfectly in agreement with the transition from the unstable to stable regime in the experiment.

To further analyze the results present in Fig. 12, we employed an edge detection technique to provide an outline of the interface (finger) and finally quantify the number, width, and length of fingers as presented in Fig. 13(a). We initially observe a progressive increase in both the length and width of the individual fingers over time. After a certain distance, buoyancy forces the fingers to stop growing in length, while all the remaining fingers keep merging, thus increasing their width. Finally, the fingers disappear and the interface becomes relatively stable.

In general, the model is found to offer a reasonable representation of the physical behaviors in the converging and diverging cells. Examples are presented in Figs. 14 and 15, wherein the measurements are taken at 70% of the way through the cell to ensure that the flow was fully developed and to avoid any repercussions of end effects on experimental data. The prediction of the spike height and length in the converging cell is very satisfactory, as can be seen in Fig. 14. The prediction of the spike height and length, as well as the front height are also reasonable for the diverging cell in Fig. 15. Finally, it is worth noting that the self-spreading profiles in highly converging cells take on a new, wedgelike shape due to buoyancy being so drastically reduced [e.g., see the last interface profiles in Fig. 9(a)].

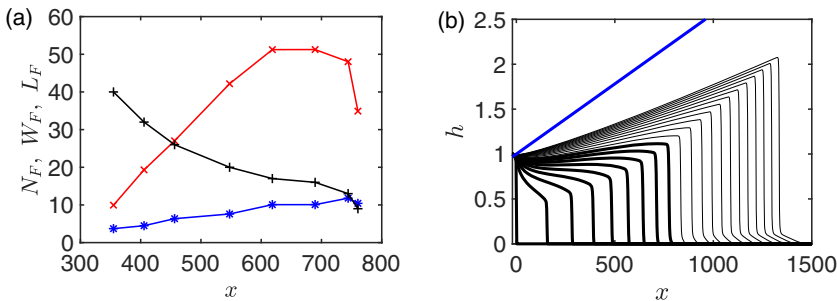


FIG. 13. Analyzing the stabilization effect for the experiment of Fig. 12. (a) Finger characteristics as time grows for $t = 25, 90, 155, 285, 415, 545, 650, 675$: number of fingers (N_F , +); average finger width (W_F , *); average finger length (L_F , x). We remind one that all lengths have been rendered dimensionless using \hat{D}_0 throughout the paper. (b) Interface profiles from simulation for $t = 0, 200, 400, \dots, 1800, 2000$, with the same parameters as in the experiment. Profiles for which the experimental flow is unstable are marked by thicker lines.

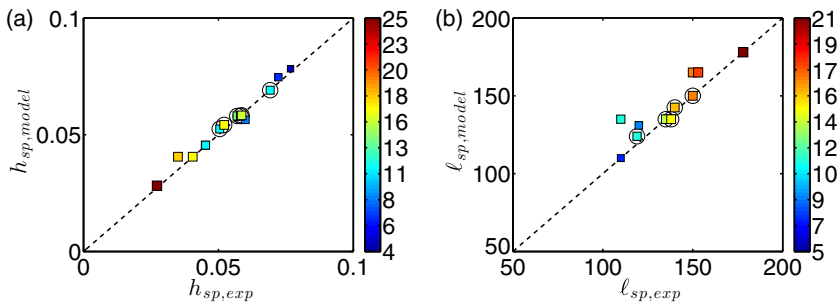


FIG. 14. Simulated versus experimental results for the spike length and height, measured at $x = 650$ in a converging cell with $\alpha L = -0.8$. Datapoints for $m = 1$ are marked by superposed circles and for $m = 10$ without. Note that, due to the wedgelike nature of the interface profiles [e.g., evident in Fig. 9(a)], comparisons of front heights were not performed for the converging geometry.

IV. SUMMARY

To summarize, our experimental and simulation results reveal that inducing a depth gradient into a Hele-Shaw cell results in a change of the transition boundaries between the three flow regimes that are well understood for a uniform Hele-Shaw cell, i.e., self-spreading, spike, and unstable flow regimes. Interestingly, the intricacies of our buoyant miscible displacement flows in a nonuniform cell can be reasonably predicted using a simple lubrication-type model that takes into account the density and viscosity ratios as well as the local geometrical variations. The results show that a cell nonuniformity allows for transitions from one regime to another: a converging cell offers a transition from spike to self-spreading or unstable regime, while a diverging cell results in a transition from self-spreading or unstable to spike regime, which provides a means to control interfacial instabilities. The results also demonstrate the importance of approaching nonuniform cell displacements as novel cases and not as extensions or variations of uniform cell flows. The constant change of balancing forces throughout the interface, which stems from the nonuniformity, means that the spatiotemporal nature of these flows must be taken into account (through solving the interface propagation equation) to achieve accurate predictions. Finally, it is important to note that a detailed stability analysis needs to be developed to shed further light on the impact of a cell nonuniformity on the stability of our displacement flows.

ACKNOWLEDGMENTS

This research has been carried out at Université Laval, supported financially by the Discovery Grant of the Natural Sciences and Engineering Research Council of Canada (NSERC) and the

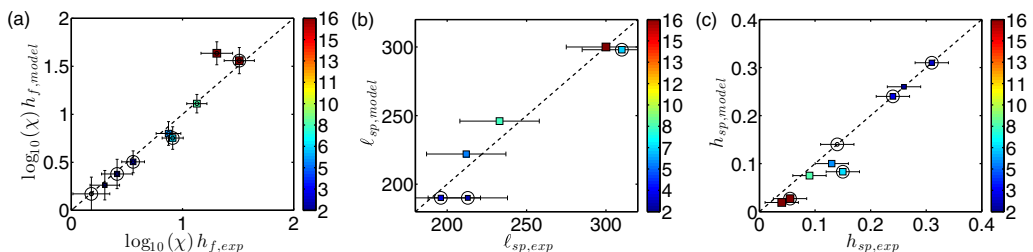


FIG. 15. Simulated versus experimental results for the front height as well as the spike length and height, measured at $x = 1150$ in a diverging cell with $\alpha L = 0.8$. Datapoints for $m = 1$ are marked by superposed circles and for $m = 10$ without.

infrastructure support provided by the Canada Foundation for Innovation (CFI). E.W. also acknowledges additional financial support through the Faculty of Science and Engineering Undergraduate Scholarship. We thank J. Noël and J. N. Ouellet (department technicians) for the construction of the experimental apparatus and useful technical discussions.

-
- [1] O. Manickam and G. M. Homsy, Fingering instabilities in vertical miscible displacement flows in porous media, *J. Fluid Mech.* **288**, 75 (1995).
 - [2] E. B. Nelson and D. Guillot, *Well Cementing* (Schlumberger, Sugar Land, 2006).
 - [3] S. Malhotra, E. R. Lehman, and M. M. Sharma, Proppant placement using alternate-slug fracturing, *SPE J.* **19**, 974 (2014).
 - [4] J. Wiklund, M. Stading, and C. Trägårdh, Monitoring liquid displacement of model and industrial fluids in pipes by in-line ultrasonic rheometry, *J. Food Eng.* **99**, 330 (2010).
 - [5] T. T. Al-Housseiny, P. A. Tsai, and H. A. Stone, Control of interfacial instabilities using flow geometry, *Nat. Phys.* **8**, 747 (2012).
 - [6] S. Hill, Channeling in packed columns, *Chem. Eng. Sci.* **1**, 247 (1952).
 - [7] R. A. Wooding, Growth of fingers at an unstable diffusing interface in a porous medium or Hele-Shaw cell, *J. Fluid Mech.* **39**, 477 (1969).
 - [8] L. Paterson, Fingering with miscible fluids in a Hele-Shaw cell, *Phys. Fluids* **28**, 26 (1985).
 - [9] J. Fernandez, P. Kurowski, P. Petitjeans, and E. Meiburg, Density-driven unstable flows of miscible fluids in a Hele-Shaw cell, *J. Fluid Mech.* **451**, 239 (2002).
 - [10] F. H. C. Heussler, R. M. Oliveira, M. O. John, and E. Meiburg, Three-dimensional Navier–Stokes simulations of buoyant, vertical miscible Hele-Shaw displacements, *J. Fluid Mech.* **752**, 157 (2014).
 - [11] G. Scovazzi, M. F. Wheeler, A. Mikelić, and S. Lee, Analytical and variational numerical methods for unstable miscible displacement flows in porous media, *J. Comput. Phys.* **335**, 444 (2017).
 - [12] R. Ramachandran, Stability and onset of two-dimensional viscous fingering in immiscible fluids, [arXiv:1704.02674](https://arxiv.org/abs/1704.02674).
 - [13] E. Lajeunesse, J. Martin, N. Rakotomalala, and D. Salin, 3D Instability of Miscible Displacements in a Hele-Shaw Cell, *Phys. Rev. Lett.* **79**, 5254 (1997).
 - [14] E. Lajeunesse, J. Martin, N. Rakotomalala, D. Salin, and Y. C. Yortsos, Miscible displacement in a Hele-Shaw cell at high rates, *J. Fluid Mech.* **398**, 299 (1999).
 - [15] E. Lajeunesse, J. Martin, N. Rakotomalala, D. Salin, and Y. C. Yortsos, The threshold of the instability in miscible displacements in a Hele-Shaw cell at high rates, *Phys. Fluids* **13**, 799 (2001).
 - [16] N. Goyal and E. Meiburg, Miscible displacements in Hele-Shaw cells: Two-dimensional base states and their linear stability, *J. Fluid Mech.* **558**, 329 (2006).
 - [17] N. Goyal, H. Pichler, and E. Meiburg, Variable-density miscible displacements in a vertical Hele-Shaw cell: Linear stability, *J. Fluid Mech.* **584**, 357 (2007).
 - [18] N. Rakotomalala, D. Salin, and P. Watzky, Miscible displacement between two parallel plates: BGK lattice gas simulations, *J. Fluid Mech.* **338**, 277 (1997).
 - [19] Z. Yang and Y. C. Yortsos, Asymptotic solutions of miscible displacements in geometries of large aspect ratio, *Phys. Fluids* **9**, 286 (1997).
 - [20] S. M. Taghavi, T. Seon, D. M. Martinez, and I. A. Frigaard, Buoyancy-dominated displacement flows in near-horizontal channels: The viscous limit, *J. Fluid Mech.* **639**, 1 (2009).
 - [21] L. Talon, N. Goyal, and E. Meiburg, Variable density and viscosity, miscible displacements in horizontal Hele-Shaw cells. Part 1. Linear stability analysis, *J. Fluid Mech.* **721**, 268 (2013).
 - [22] X. Meng and Z. Guo, Multiple-relaxation-time lattice Boltzmann model for incompressible miscible flow with large viscosity ratio and high Péclet number, *Phys. Rev. E* **92**, 043305 (2015).
 - [23] R. Mollaabbasi and S. M. Taghavi, Buoyant displacement flows in slightly non-uniform channels, *J. Fluid Mech.* **795**, 876 (2016).

- [24] H. Thomé, M. Rabaud, V. Hakim, and Y. Couder, The Saffman–Taylor instability: From the linear to the circular geometry, *Phys. Fluids A* **1**, 224 (1989).
- [25] H. Zhao, J. Casademunt, C. Yeung, and J. V. Maher, Perturbing Hele-Shaw flow with a small gap gradient, *Phys. Rev. A* **45**, 2455 (1992).
- [26] E. O. Dias and J. A. Miranda, Finger tip behavior in small gap gradient Hele-Shaw flows, *Phys. Rev. E* **82**, 056319 (2010).
- [27] T. T. Al-Housseiny and H. A. Stone, Controlling viscous fingering in tapered Hele-Shaw cells, *Phys. Fluids* **25**, 092102 (2013).
- [28] E. O. Dias and J. A. Miranda, Control of centrifugally driven fingering in a tapered Hele-Shaw cell, *Phys. Rev. E* **87**, 053014 (2013).
- [29] R. Brandão, J. V. Fontana, and J. A. Miranda, Suppression of viscous fingering in nonflat Hele-Shaw cells, *Phys. Rev. E* **90**, 053003 (2014).
- [30] D. Pihler-Puzović, P. Illien, M. Heil, and A. Juel, Suppression of Complex Fingerlike Patterns at the Interface Between Air and a Viscous Fluid by Elastic Membranes, *Phys. Rev. Lett.* **108**, 074502 (2012).
- [31] D. Pihler-Puzović, R. Périllat, M. Russell, A. Juel, and M. Heil, Modelling the suppression of viscous fingering in elastic-walled Hele-Shaw cells, *J. Fluid Mech.* **731**, 162 (2013).
- [32] Z. Zheng, H. Kim, and H. A. Stone, Controlling Viscous Fingering Using Time-Dependent Strategies, *Phys. Rev. Lett.* **115**, 174501 (2015).
- [33] S. J. Jackson, H. Power, D. Giddings, and D. Stevens, The stability of immiscible viscous fingering in Hele-Shaw cells with spatially varying permeability, *Comput. Methods Appl. Mech. Eng.* **320**, 606 (2017).
- [34] L. Ducloué, A. L. Hazel, D. Pihler-Puzović, and A. Juel, Viscous fingering and dendritic growth under an elastic membrane, *J. Fluid Mech.* **826**, R2 (2017).
- [35] A. Eslami, I. A. Frigaard, and S. M. Taghavi, Viscoplastic fluid displacement flows in horizontal channels: Numerical simulations, *J. Non-Newtonian Fluid Mech.* **249**, 79 (2017).
- [36] A. Eslami and S. M. Taghavi, Viscous fingering regimes in elasto-visco-plastic fluids, *J. Non-Newtonian Fluid Mech.* **243**, 79 (2017).
- [37] H. C. Yee, R. F. Warming, and A. Harten, Implicit total variation diminishing (TVD) schemes for steady-state calculations, *J. Comput. Phys.* **57**, 327 (1985).
- [38] S. M. Taghavi, R. Mollaabbasi, and Y. St-Hilaire, Buoyant miscible displacement flows in rectangular channels, *J. Fluid Mech.* **826**, 676 (2017).
- [39] N. S. Cheng, Formula for the viscosity of a glycerol-water mixture, *Ind. Eng. Chem. Res.* **47**, 3285 (2008).